Scalable 3-D-Printable Antenna Array With Liquid Cooling for 28 GHz

Jaakko Haarla, Juha Ala-Laurinaho, and Ville Viikari, *Senior Member, IEEE*

***Abstract*— This article presents a scalable and compact 3-D-printed Vivaldi antenna array with liquid cooling for the frequency band from 24.0 to 29.5 GHz. The proposed design consists of an 8 × 8 antenna array with commercial beam-forming integrated circuits (ICs) on the antenna side of the PCB for efficient PCB area utilization that enables a high integration level. Scalable liquid cooling is integrated into the 3-D-printed antenna array. The measured temperature with water cooling during operation remains below 50 °C. The simulated total active reflection coefficient (TARC) of the unit cell is lower than −9.6 dB for beam steering angles up to 57° from the broadside. The effective isotropic radiated power (EIRP) of the prototypes is up to 59.7 dBm.**

***Index Terms*— 3-D-printable antennas, active arrays, beam steering, electronics cooling, millimeter-wave antenna arrays, Vivaldi antenna array.**

I. Introduction

THE demand for higher data transfer rates is pushing the adaption of new wireless technologies and the use of higher frequency ranges in mobile network systems [1], [2]. Beam steering is currently used as part of the solution to maintain wide coverage with the narrow beams of the high-gain antennas.

A common solution is an antenna array with multichannel vector modulators [radio-frequency integrated circuits (RFICs)] to enable beam steering. The state-of-the-art solutions use, for example, patch arrays [3], [4], [5], [6], [7], [8], [9] and Vivaldi arrays [10], [11], [12], [13] as antenna elements. Millimeter-wave antenna arrays, however, have inherent challenges with RFIC integration. As the frequency increases, the antenna-element size and interelement distance are reduced to a level comparable to the RFIC size. This presents two problems as follows.

1) The heat generated by the RFICs is concentrated in a smaller area. Furthermore, the efficiency of the active RFICs decreases as the frequency increases [14], leading to increased thermal output.
2) The limited space is available for RFIC and antenna elements on the PCB that demand high-density integration.

Normally, the previously mentioned problems are solved by moving the RFICs to the back side of the PCB and using the available space on the back side for large heat sinks and cooling fans. This approach works thermally but has some downsides: the space utilization is not efficient as the back side of the PCB is occupied by the RFICs and cooling solution and therefore the integration of other electronics is challenging. The RFIC control and bias lines need to be embedded in a multilayer PCB, and the RF signal needs to be routed through the PCB, which can be challenging and increase the overall complexity of the PCB. As a consequence, the remaining functionalities, such as baseband electronics, frequency conversions, and power distribution need to be realized on separate PCBs. Multiple PCBs are connected using bulky and complex connectors and lines.

The concept of locating RFICs on the antenna side of the PCB while retaining the cooling on the backside has been introduced but was demonstrated at a lower frequency [15], [16]. This simplifies the RF routing but introduces restrictions to the cooling capability since heat is conducted through the PCB.

Liquid cooling has been demonstrated in a phased array where the LTCC (PCB equivalent) is patterned to realize embedded cooling channels [17], [18]. A narrow-band patch antenna array is realized on the front side of the PCB, and the RFICs are mounted on the back side in a typical manner. Research has been done on the use of 3-D-printed or machined metal antennas used as a heat sink on a smaller scale [19], [20], [21] or at lower frequencies [22]. However, small-scale arrays with few RFICs do not demonstrate the thermal challenges properly. In small arrays, all RFICs are located on the outer edge, leaving lower thermal conductance, higher thermal capacity, and more surface area for heat dissipation. As the array size increases, the heat concentration problem worsens.

The concept of liquid-cooled metal antenna arrays has been introduced for sparse antenna arrays [23]. However, an open-ended waveguide design leads to a relatively large element size and, thus, limits the beam-steering range. Furthermore, the article introduces only the initial concept without showing the full-scale demonstration.

We introduce a fully functional design and prototype to solve the mentioned space utilization and excessive heating problems. We have designed a dense 2-D Vivaldi antenna array featuring a wide beam-steering capability with an embedded liquid-cooling system. The design is realized as a single 3-D-printed metal block, and the whole array is mounted on the PCB as a single element. The connectorless interface between the array and the PCB does not require solder. The proposed design (see Fig. 1) moves the antenna elements away from the PCB and uses a slim slotline transition for the

Manuscript received 15 September 2022; revised 24 February 2023; accepted 21 March 2023. Date of publication 10 April 2023; date of current version 2 June 2023. This work was supported in part by the Business Finland Project RF Sampo under Grant 3071/31/2021. *(Corresponding author: Jaakko Haarla.)*

The authors are with the Department of Electronics and Nanoengineering, Aalto University, 02150 Espoo, Finland (e-mail: jaakko.haarla@aalto.fi).

Color versions of one or more figures in this article are available at https://doi.org/10.1109/TAP.2023.3264861.

Digital Object Identifier 10.1109/TAP.2023.3264861

This work is licensed under a Creative Commons Attribution 4.0 License. For more information, see https://creativecommons.org/licenses/by/4.0/

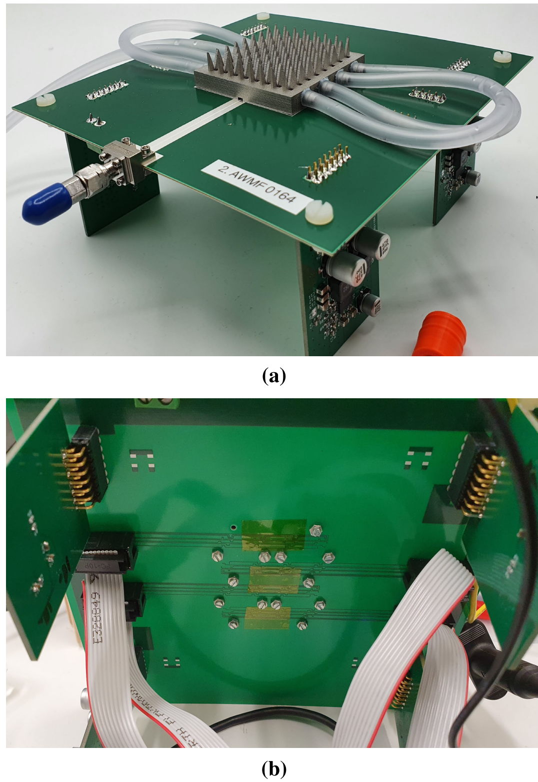

Fig. 1. (a) Three-dimensional printable antenna array with liquid cooling showing the manufactured prototype with cooling pipes and power supplies. (b) Back side of the prototype shows the absence of RF components and cooling.

RF connection. Thus, the RFICs can be located on the front side of the PCB between the slotline transitions. Furthermore, the 3-D-printed block has embedded cooling channels located on top of the RFICs that enable efficient heat transfer. The prototype uses water as the coolant.

Our prototype utilizes only the front half of the PCB stackup (three layers) for the RF section, which simplifies the PCB stackup and routing compared to the dual-sided version. All traces on the back half of the PCB stackup are control signals and power planes that can be trivially rearranged. The back side of the PCB (apart from attachment bolts) is thus open to being used by any other RF/non-RF circuitry, like power supplies or field-programmable gate arrays (FPGAs), as seen in Fig. 1(b). A novel ridged-waveguide transition section between the PCB and the Vivaldi array makes fitting the cooling channels in the structure possible.

The antenna array consists of 3-D-printed Vivaldi elements. The proposed design covers the 24-GHz industrial, scientific, and medical (ISM)-band and the following 5G new radio (NR) FR2 bands: n257, n258, and n261 [24]. Altogether, these bands cover the frequency band between 24.0 and 29.5 GHz.

The following are the novelties of the proposed design.

1) The 3-D-printed liquid-cooled antenna array is used to manage the RFIC temperature at 24.0–29.5 GHz.
2) The RFICs and all RF traces are located on the antenna side of the PCB.
3) The back side of the PCB remains free for electronics.
4) The solderless ridged waveguide transition between the PCB and the 3-D-printed antenna enables a connectorless interface and leaves room for cooling channels.
5) The compact feed network including the balun and back-cavity is realized on the PCB. The back-cavity on the PCB simplifies the 3-D Vivaldi array structure significantly and enables a ridged-waveguide transition.

The proposed design has also other advantages including: a fully scalable RF and thermal design and a simple six-layer PCB stackup.

The concepts behind the prototype are introduced in Section II, and the prototype-specific details are explained in Section III. The simulation and measurement results are presented in Section IV. The results are discussed in Section V, and the article is concluded in Section VI.

II. Design

The interelement distance, an important design parameter, affects the array gain and grating lobe-free beam-steering range. A grating-lobe-free beam-steering up to θ is ensured when

$$d < \frac{c_0}{f_{\mathbf{max}}} \frac{1}{1 + |\sin\theta|} \quad (1)$$

where c_0 is the speed of light, θ is the largest steering angle, and $f_{\mathbf{max}}$ is the highest operation frequency. Grating lobes can result in higher interference and lowered gain as a large portion of the energy is transmitted to the grating lobe.

Equation (1), however, does not guarantee good beam-steering performance for smaller arrays. The width of the grating lobe depends on the antenna size. In practice, the maximum steering angle is smaller since the side of the grating lobe enters the visible area before the peak in finite arrays. The active reflection coefficient can also degrade when the grating lobe becomes visible [25].

The selected RFIC imposes a major design constraint on the prototype. We designed the prototype around two commercial four-channel beam-former RFICs: Anokiwave AWMF-0158 and AWMF-0164. These RFICs have identical dimensions and layouts while providing different frequency bands (24.25–27.5 and 26.5–29.5 GHz). The ISM frequency band (24.0–24.25 GHz) is included in the antenna design and the simulations. Thus, the proposed antenna design covers the frequency band from 24.0 to 29.5 GHz. Two identical antenna arrays were manufactured with the only difference being that they are equipped with different beam-former chips, one supporting the band 24.25–27.5 GHz and the other the band 26.5–29.5 GHz.

The antenna-element spacing is calculated to be 5.45 mm using (1) with $f_{\mathbf{max}} = 29.5$ GHz and $\theta = 60°$. We made the design a little more compact and used a spacing of 5.35 mm in the prototype. This decreases the visible parts of the grating lobes for large steering angles. This antenna spacing allows beam-steering up to 40° without the appearance of grating lobes, and at 60°, the grating lobes remain weaker than the main beam.

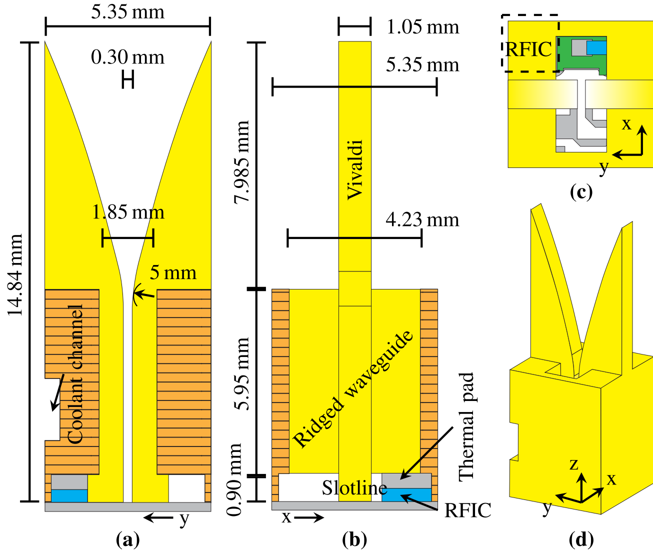

Fig. 2. (a) and (b) Orthogonal cuts of the Vivaldi unit-cell model. (c) Top view and (d) side view of the unit cell. The space reservation for the coolant channel is seen in (a) and (d).

In the proposed design, the RFIC, the bypass capacitors, and the signal distribution network are located on the same side of the PCB as the antennas. This requires a co-design between the 3-D-printed antenna element and the corresponding PCB layout to achieve the specified antenna spacing.

A. Unit Cell of the 3-D-Printed Antenna

A unit-cell simulation of a single Vivaldi antenna element is shown in Fig. 2. The shape of the radiating Vivaldi section is a curve defined by equations [26]

$$c_1 = \frac{y_2 - y_1}{e^{Rz_2} - e^{Rz_1}} \tag{2}$$

$$c_1 = \frac{y_1 e^{Rz_2} - y_2 e^{Rz_1}}{e^{Rz_2} - e^{Rz_1}} \tag{3}$$

$$y = c_1 e^{Rz} + c_2 \tag{4}$$

where $y_2 = 2.675$, $y_1 = 0.15$, $z_2 = 7.985$, $z_1 = 0$, and $R = 0.866$. The thickness of the Vivaldi is 1.05 mm. The Vivaldi section is connected to the PCB with a 5.95-mm-long ridged waveguide and a 0.9-mm-long slotline. A bend with a radius of 5 mm is introduced in the interface between the Vivaldi and the ridged waveguide. The dimensions of the ridged waveguide are 4.23 and 1.85 mm, and the ridge width is equal to the Vivaldi element thickness of 1.05 mm, and the gap is 0.3 mm.

The ridged waveguide utilizes only 1.85 mm of the unit cell width in the y-direction [see Fig. 2(a)]. The remaining cross section is solid metal. The solid part on top of the RFIC can be utilized for the cooling channel that passes through the unit cell along the x-axis, whereas the opposite side is reserved for 1.6-mm (M1.6) threads. These embedded features inside the solid metal can be freely modified as long as the surface of the rigid waveguide remains intact. The 3-D-printed antenna array was manufactured with digital metal. The 3-D-print material is 316L stainless steel (conductivity of $1.32 \cdot 10^6$ S/m and surface roughness rms of 3.3 μm) [27], [28].

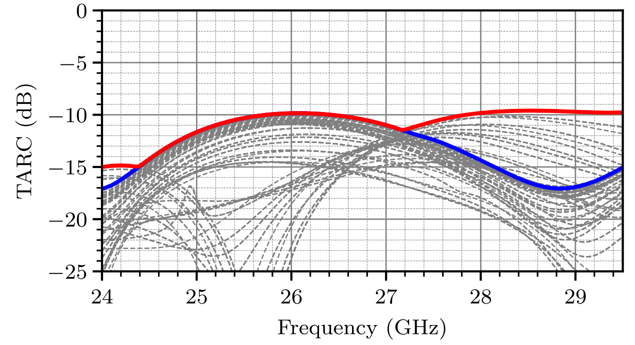

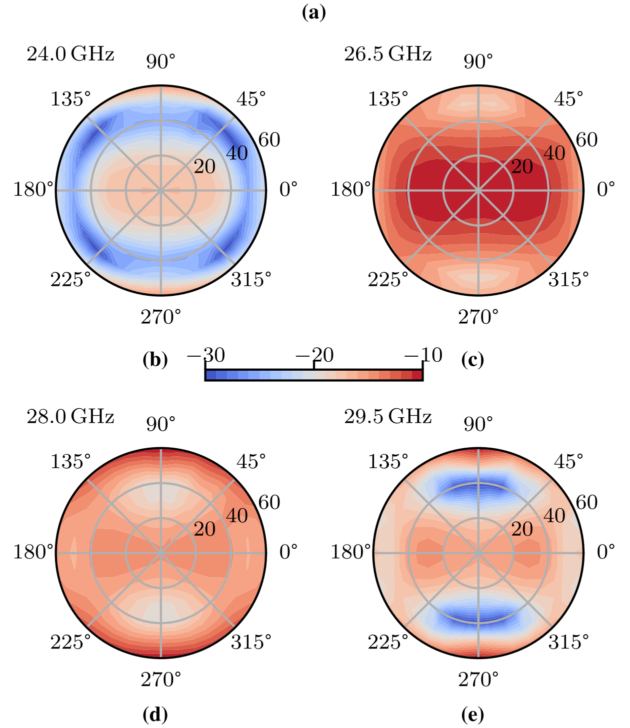

Fig. 3. TARC for the beam-steering angles ($0° < \phi < 360°$ and $0° < \theta < 60°$). (a) TARC of all simulation cases in dashed gray, broadside ($\theta = 0°, \phi = 0°$) in blue, and the envelope curve in red. (b)-(e) TARC as a function of the steering angle at the specified frequency.

The structure of the individual antenna element is simulated and optimized using the CST Microwave Studio unit-cell simulation, which assumes an infinite array and can approximate the operation of finite arrays [29]. The simulation includes the PCB feed section, which is presented below.

The unit cell is simulated for angles from broadside up to 60° and around the normal of the antenna in 10° steps. Fig. 3 shows the simulated total active reflection coefficients (TARCs). The envelope TARC is −9.6 dB or lower over all simulated angles, and the frequency range is from 24.0 to 29.5 GHz. The antenna structure is optimized to provide the best TARC over all beam steering angles and over the whole operational frequency band. Thus, the best TARC is not necessarily achieved toward the broadside.

The active element pattern (AEP) is calculated for the unit cell model. Fig. 4 shows an ideal cosine function and the E-, H-, and D-plane cuts from the AEP at 24.0, 26.5, 28.0, and 29.5 GHz. The AEP shows a near-cosine-like behavior in the E-, H-, and D-plane for the proposed element.

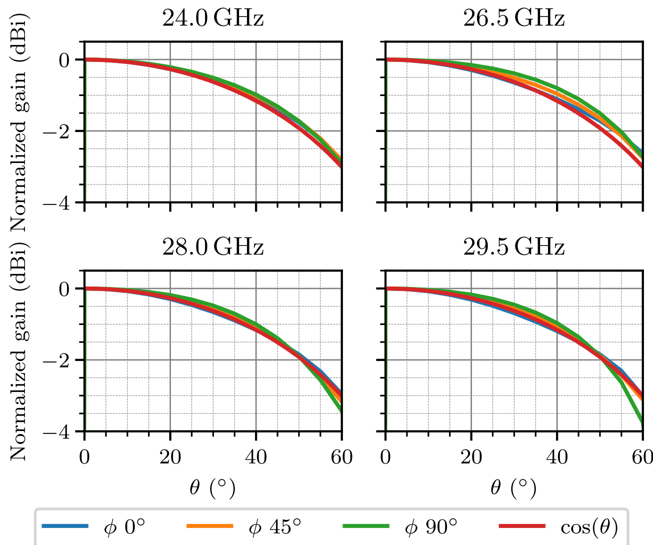

Fig. 4. AEP cuts in the E-, H-, and D-planes ($\phi = 0°, 45°, 90°$).

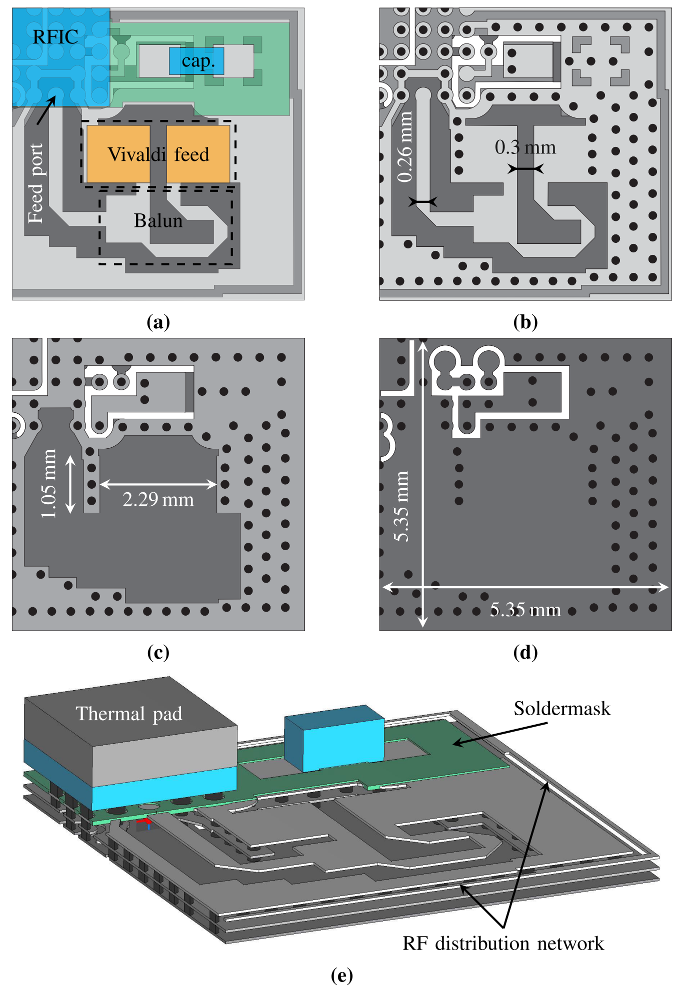

Fig. 5. (a) PCB layout in the unit cell. The RF copper layers are shown from the top down: (b) L1, (c) L2, and (d) L3. (e) Three-dimensional model with a transparent substrate.

B. PCB

The proposed 3-D-printed antenna array is a surface-mountable module that is pressed against the PCB. Thus, the PCB is designed simultaneously with the antenna array to ensure a good electrical and thermal interface between them.

The designed unit-cell PCB with the most important dimensions and the layout is shown in Fig. 5. The design files are provided separately for more dimensional details [30]. The footprint of the individual antenna element on the PCB is restricted by the antenna spacing. Since the balun and the back-cavity of the Vivaldis are wavelength-based elements, a high-dielectric-constant substrate is needed. The stackup of the PCB consists of an FR-4 core with two 4460G2 prepregs on both sides for symmetry during manufacturing [see Fig. 6(b)]. Two stacked 101-μm-thick Rogers 4460G2 with a dielectric constant of 6.15 and loss tangent of 0.0038 reduces the dimensional requirements by 43% compared to the common Rogers 4350B (dielectric constant of 3.48). This leaves enough space for an additional ground ring added around the antenna element [see Fig. 5(b) and (c)]. The ground ring improves the isolation between the antenna elements on the PCB and prevents leakage to the RF distribution network, control lines, and dc power planes. Smaller spatial requirements for the balun allow the RF distribution network to be routed between the antenna elements. The RF distribution network is visible on the edge of the unit cell in Fig. 5(a), (b), and (e).

The thickness of the copper sheets in the simulations is 35 μm with conductivity 4.76×10^7 S/m and surface roughness rms 0.5 μm. An extensive via-stitching [seen, e.g., in Fig. 5(b)] is used between the L1–L3 ground planes where allowed by the PCB manufacturer design rules. The feed port for the antenna is located under the RFIC's ball-grid array pad. A 50-Ω microstrip line is routed to the other side of the unit cell, where it is converted to a differential microstrip with a $\lambda/4$ balun and then connected to the ridged waveguide via a slot line.

The Vivaldi's back-cavity is formed under the ridged waveguide section by terminating the outer edges of the ridged waveguide to the L3 ground plane with three vias on each side. The distance between the termination vias is 2.29 mm. The termination to the L3 ground plane removes the need for additional structures behind the PCB and allows the back side of the PCB to be used, for example, for control and LO signals.

The RFIC is modeled as a silicon ($\epsilon_{\text{silicon}} = 11.9$) slab, and the heat pad connecting the RFIC to the 3-D-print as a rubber ($\epsilon_{\text{rubber}} = 3.0$) slab in the simulation due to their proximity to the antenna.

C. Distribution Network

A tree-like network distributes the signals from the edge of the antenna array to the RFICs. The array is arranged into submodules, each powered by one RFIC. Each submodule consisting of an RFIC and four antenna elements is arranged so that it does not interfere with the tree-like distribution network [see Fig. 6(a)]. Unlike the antenna traces between layers L1 and L3, the distribution network utilizes conductor-backed coplanar waveguides and uses only the outer 4460G2 prepreg (between L1 and L2) to minimize size requirements. Thus, all RF traces can be routed on one side of the PCB.

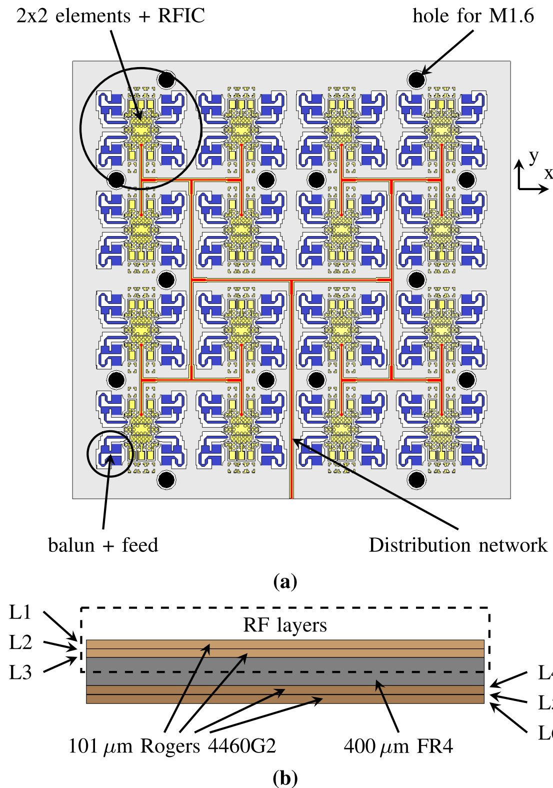

Fig. 6. (a) RF-traces on the PCB. The antenna feeds are marked in blue, the distribution network in red, and the holes for the mounting of the 3-D structure in black. (b) PCB stackup.

The signal distribution from the edge of the antenna array to the RFICs is simulated in an EM simulator. The tree-like distribution network utilizes T-junctions with $\lambda/4$-transformers (length $=$ 1380 μm, width $=$ 225 μm) for equal signal distribution. The insertion loss for each signal line is between 15.0 and 15.8 dB over the entire frequency range. The theoretical loss for power splitters is 12 dB. Thus, the power loss within the materials is 3.0–3.8 dB. The manufactured prototype has an additional conductor from the edge of the antenna array to the end-launch connector on the edge of the prototype PCB. The transition is simulated separately, and the results are added to the feed network simulation. The total insertion loss is 6.1–7.2 dB between the RF edge connector and the RFIC input.

D. Thermal Considerations

The thermal properties of a large antenna array are subject to the same size limitations as the antenna unit cells. As the array size increases, the individual unit cell is surrounded by similar antennas with similar heat production and dissipation. The surrounding elements are at the same thermal potential, and thus the individual element can dissipate heat only along the normal of the antenna array. Hence, the needed cooling capacity can be modeled with a rectangular block representing an RFIC, the corresponding antenna structure with four walls as ideal thermal insulators, and the top and the bottom as heat flux simulating natural convection from metal to air. The heat source is added to the bottom side to simulate active electronics on one side of the antenna array. The thermal simulations are done with the multiphysics simulator COMSOL.

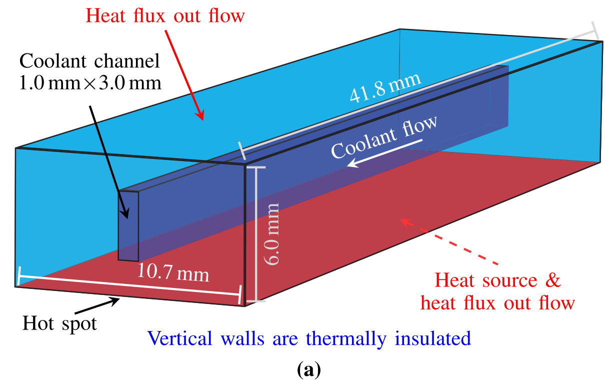

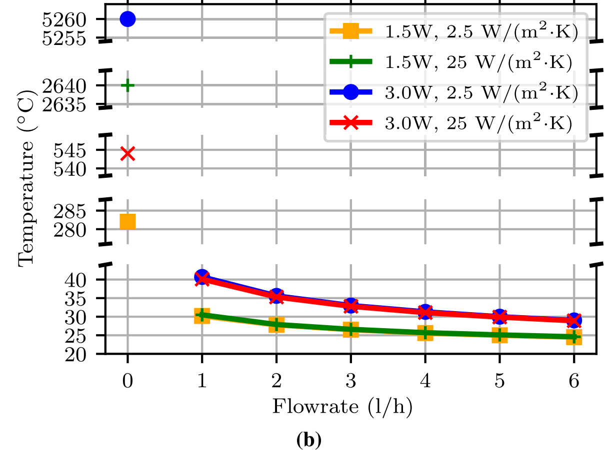

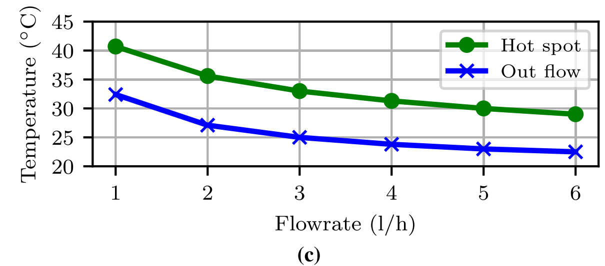

Fig. 7. (a) Simple thermal model for cooling for comparison with the water-filled cooling channel in the middle. (b) Hot-spot temperature as a function of the coolant flow rate for two metal-to-air heat flux values. (c) Temperature of the structure hot spot and the average temperature of the coolant outflow with respect to the flow rate.

Since each RFIC feeds the 2×2 antenna configuration, we simulated an 8×2 block and added a heat source corresponding to four RFICs. The simulation block dimensions are $41.8 \times 10.7 \times 6.0$ mm with a $41.8 \times 1.0 \times 3.0$-mm-sized channel for the liquid cooling. The model is shown in Fig. 7(a). The four vertical walls of the model are thermally insulated. The top side and the bottom side of the model are modeled as a heat flux with a corresponding heat transfer coefficient of 2.5 or 25.0 W/(m^2·K). The natural heat convection heat flux is between these values based on the literature [31]. Additionally, the heat source (4×1.5 W or 4×3.0 W) is assigned to the bottom side of the model.

The simulations are done in two stages. The first stage tests the natural convection rate without any liquid cooling (the flow

rate is 0) and the second stage is the same simulation with a nonzero flow rate for the liquid.

Based on our measurements, the power consumption of a single RFIC is 1.5 W. For additional margin, we used 3.0 W as the heat generation power of a single beam-former chip in the simplified thermal simulations.

The simulations show that, without liquid cooling, the steady-state temperatures for the theoretical model range from 282 °C to 5260 °C, which are far too high since the typical maximum operation temperature of electric components is in the order of 85 °C. When liquid cooling is applied, the temperature reduces drastically, as shown in Fig. 7. When a 20 °C, 1 l/h coolant circulation is introduced into the system with 12-W dissipated power, the hot-spot temperature decreases to 40 °C. The hot-spot temperature mainly follows the liquid flow rate, and the effect of the natural convection from surfaces diminishes rapidly, as seen in Fig. 7(b). Fig. 7(c) shows the hot-spot temperature and the average temperature of the out-flowing liquid as a function of the flow rate. The decreasing hot-spot temperature indicates that the further increase in inflow increases the cooling capability of the system. The difference between the hot spot and the average outflow temperature remains approximately the same.

Since the difference between inflow and outflow average temperature remains low at higher flow rates, the structure can be scaled for much longer cooling channels while maintaining a low coolant temperature along the whole structure. For example, with a flow rate of 3 l/h, the coolant heats up by 5 °C, and the hot spot is 8 °C above the coolant. If four models are added in series, the hot-spot temperature is four times the coolant temperature increase plus the temperature difference between the coolant and the hot-spot ($4 \cdot 5$ °C + 8 °C = 28 °C). Thus, the hop-spot temperature would be 28 °C above the inflow coolant temperature.

We can conclude that the liquid-cooling solution is necessary and that a single 1.0 × 3.0 mm channel is enough for each line of RFICs in our prototype. A more detailed analysis of the prototype is discussed in Section III.

III. Proposed Prototype

The proposed prototype consists of two main parts: The 3-D-printed antenna array and the RF-PCB for the electronics. Both parts and the attached coolant tubes are shown in Fig. 1. In addition, the prototype includes four switching power supplies and an external control board. Each power supply board provides 1.8 and 2.5 V rails to a set of four RFICs. All RFICs are controlled by an Arduino-based control board. The prototype is presented in more detail in Sections III-A and III-B.

A. 8 × 8-Element Array

The proposed 3-D-printed antenna array shown in Fig. 8(a) consists of an 8 × 8 configuration of previously described Vivaldi antennas that are fed using ridged waveguides. These waveguides go through the main body of the antenna and exit the PCB side as a slot line that is pressed against the RFIC-PCB. The ridged-waveguide design allows the realization of all antenna elements and cooling structures in a single rigid metal piece.

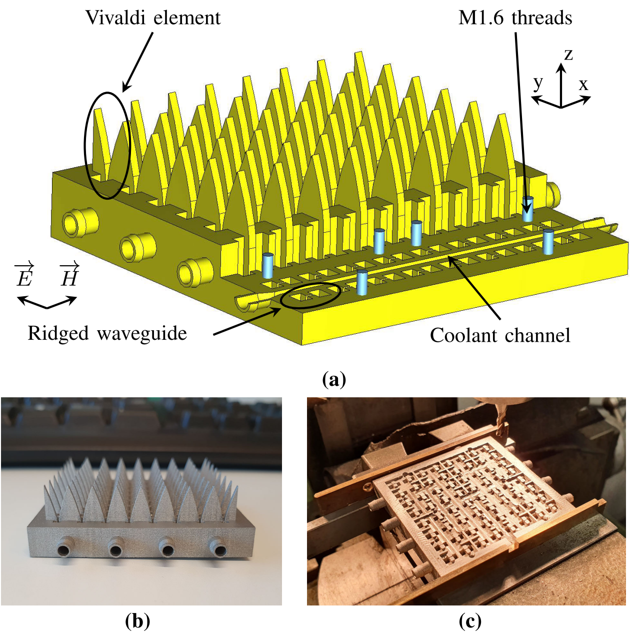

Fig. 8. (a) Three-dimensional antenna-array model with a cutout to show the coolant channel and M1.6 threads. (b) Side and (c) bottom views of the manufactured prototype.

Thick connecting structures are formed in the y-axis direction between the antenna elements. Half of them are located above the RFICs and the other half are on top of the feedline network. These thicker metal structures are used for antenna cooling and antenna attachment. The metal structures above the RFICs are hollowed and act as coolant channels with additional extensions outside the antenna for a cooling pipe attachment. The metal structures above the feeding network are used to attach the 3-D-printed antenna to the PCB. The tree-like feed network does not utilize all sections between the elements leaving unutilized space. These parts are used for M1.6-sized threaded holes. As the M1.6 bolt must go through the PCB, a keep-out area needs to be considered in the PCB layout. The PCB side of the antenna needs to have a clearance for the RFICs, decoupling capacitors, and the feeding network. The designed antenna should have a 0.9-mm clearance to the PCB surface everywhere except near the antenna feed slot lines, support structures, and the ground ring around the RF section. This clearance is seen in Figs. 8(c) and 9(b).

The full 8 × 8 antenna array is simulated in the EM simulator. Due to the finite array, the edge elements behave differently than the elements in the middle [32]. As the array size is expanded, the performance of the array approaches that with the unit-cell type elements. However, in the finite array, the total performance of the antenna array cannot be accurately evaluated based on the performance of an individual element.

The EM simulation model of the 3-D-printed antenna array is simplified by excluding the coolant connectors on the sides of the array. The first three layers of the RF-PCB are included in the array simulation. The feeding ports are located on the RFIC footprint pads. The RF-PCB outside the 3-D-print perimeter is replaced by an infinite ground plane in the

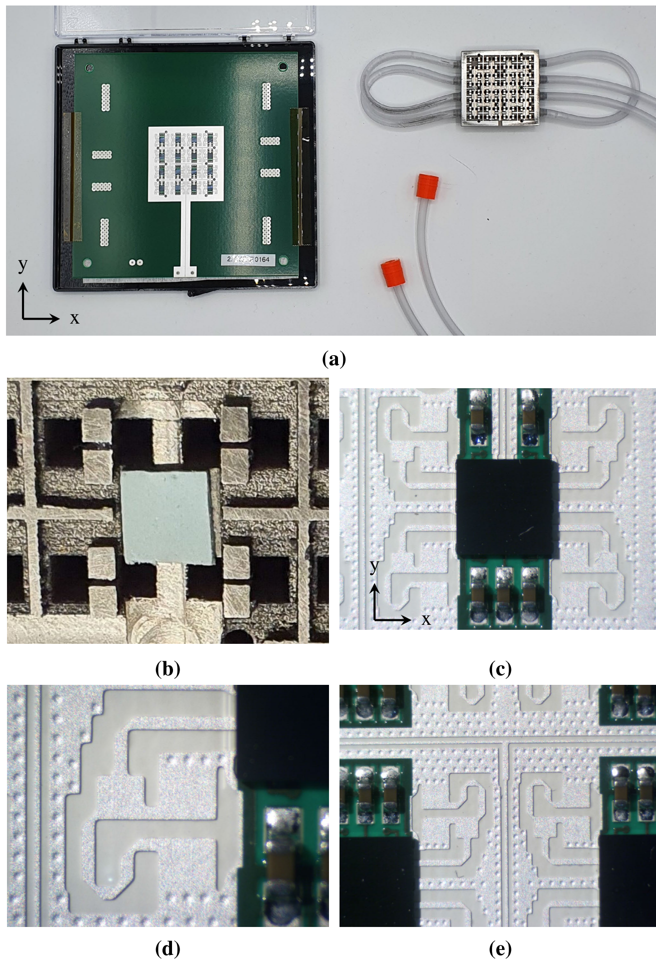

Fig. 9. (a) RFIC-PCB and the 3-D-printed antenna part with attached cooling pipes. (b) Section of the 3-D-printed prototype for one RFIC with four antenna elements and a thermal pad. (c) Corresponding RFIC with four antenna feed sections and the decoupling capacitors. (d) Single antenna feed section. (e) T-junction of the tree-like distribution network is located between antenna elements.

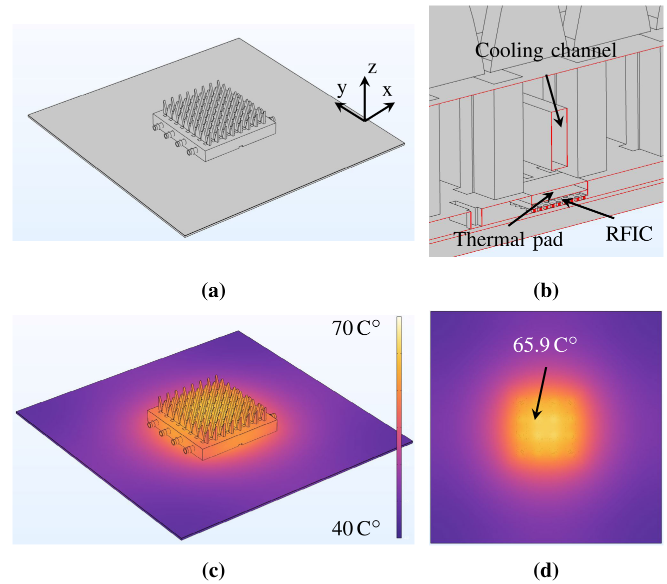

Fig. 10. (a) Full 3-D prototype in a COMSOL thermal simulation. (b) The cooling channel, the heat pad, and the RFIC stackup are in detail. The low-power (12.83 W) steady-state temperature simulation results without liquid cooling from the (c) front and (d) back.

simulation boundary box. The simulation results are compared to the measurements in Section IV-B.

B. Thermal Performance of the Antenna Array

The proposed design has 16 RFICs. Due to the close mutual proximity of the RFICs, thermal management has to be taken into account in the design. The proposed design [see Fig. 10(a)] is simulated in COMSOL. The full model simulations are performed with power levels equivalent to the corresponding measurement of the manufactured prototype.

Since the metallic 3-D-printed antenna array is located on the same side of the PCB as the RFICs, the cooling of the RFICs can be integrated into the antenna structures. The antenna structure is designed to come close to the RFIC, and a thermally conductive pad (0.5-mm-thick T-Global TG-A1250) is used to conduct heat from RFIC to the metallic structure, as shown in Fig. 10(b). The copper traces and vias are used to transfer heat from the RFIC to the opposite side of the PCB. The PCB for thermal simulations is modeled as a 0.2-mm copper layer and a 1.0-mm FR4 layer. The liquid cooling channels are integrated into the 3-D printed metallic antenna by adding a series of embedded channels in the structure. These channels are lined up between the antennas and are located on top of the RFICs. The barb connectors for inflow and outflow are located on opposite sides of the array. The Vivaldi-type antenna elements also provide increased surface area for thermal dissipation by natural convection.

Due to the complex shape, the heat transfer due to natural convection is simulated as a single fixed value at all surfaces facing ambient air. The heat flux is solved using a measured steady-state temperature from the back side of the prototype PCB without liquid cooling. Here, relatively low power is used to enable comparisons between the simulation and measurement results without the liquid cooling. The dissipated heat is approximated as 12.83 W based on 14.26-W input power and 90% power supply efficiency. The measured PCB temperature is 65.8 °C. The heat flux is adjusted in the simulation until the steady-state matches the measurements [see Fig. 10(c) and (d)]. The heat flux is calculated to be $h = 9.6$ W/(m^2·K), which fits well within the typical values ranging from 2.5 to 25 W/(m^2·K) [31].

The cooling channels are connected in series using thermal and pressure boundary conditions to simulate the same cooling configuration as in the prototype [see Fig. 9(a)]. Recirculation of the coolant creates temperature gradients throughout the prototype that can be seen in the thermal simulation results with a water flow rate of 1.26 l/h and dissipated heat power of 25.1 W [see Fig. 11(a)–(c)]. Fig. 11(d) shows the cross section of one RFIC. The thermal simulation and measurement results are presented in Section IV-C.

IV. Prototype Simulations and Measurements

The manufactured 8 × 8 antenna array is measured using an NSI planar near-field scanner. The measurement setup, shown in Fig. 12, utilizes a small submersible pump and a water

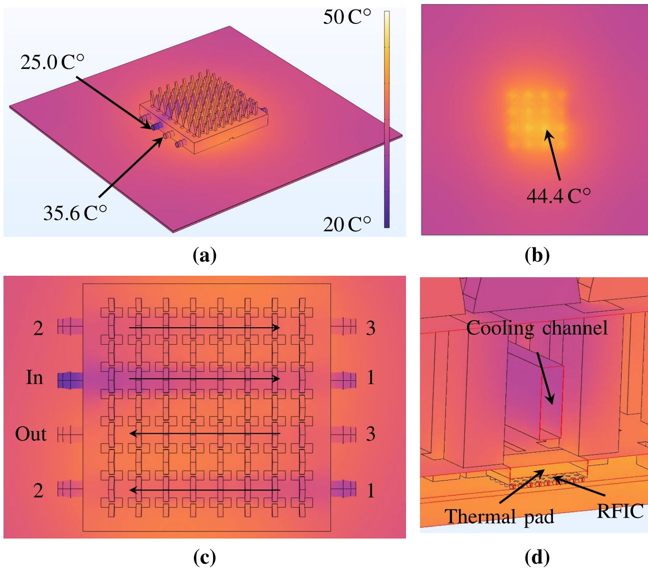

Fig. 11. COMSOL thermal simulation with flowing coolant shown from the (a) front and (b) back. (c) Cooling channel boundary conditions and flow directions. (d) Cross section of a single RFIC, thermal pad, and cooling channel. Flowrate = 1.26 l/h, dissipated heat = 25.1 W.

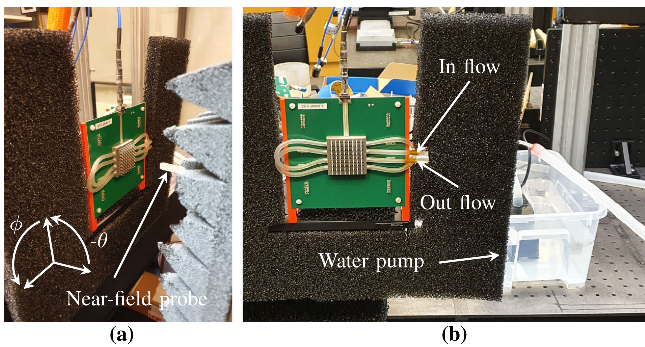

Fig. 12. Near-field measurement and cooling setups from (a) side and (b) front.

reservoir for liquid cooling. The cooling water is circulated from the pump to the prototype via a flow control valve. The flow rate is measured from the return line by sampling the volume in the measured time. The power consumption is logged by a benchtop power supply that provides 14 V to the prototype. The temperatures are recorded with a data logger and three thermal pairs (inflow, outflow, and PCB hot spot).

This section includes the phase calibration of the array, the simulation and measurement results for the 8 × 8 array, and the thermal measurements of the array.

The measured frequency range is limited by the RFIC. One of the RFICs operates between 24.25 and 27.5 GHz and the other between 26.5 and 29.5 GHz. Otherwise, both these measurements use identical 3-D-printed antenna arrays and PCBs.

A. Back-Propagation-Based Calibration Values

Single-element radiation patterns are measured first. The TX (transmit) amplifier is turned on for a single element, and the near-field scan at a distance of 50 mm from the antenna is performed. This is repeated for all elements in the array. The phase of a single element is approximated by back-propagating the measured near field to the antenna plane and calculating

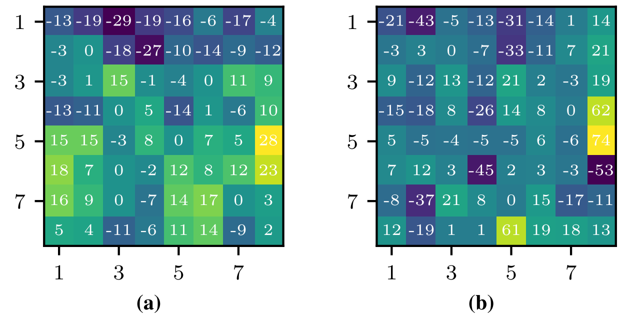

Fig. 13. (a) Phase variation of each element from the average in the array for Prototype 1 at 25.5 GHz and (b) for Prototype 2 at 28.0 GHz.

the phase for the maximum amplitude point. The calibration is performed at a single frequency in each prototype: for Prototype 1 at 25.5 GHz and for Prototype 2 at 28.0 GHz. These values are given in Fig. 13. The phase is referenced to the average of the corresponding dataset. By introducing an opposite, element-wise phase offset, the phase errors in the array can be compensated.

B. Antenna Array Simulation and Measurement Results

In all the 8 × 8-antenna array simulations, the antenna elements are fed with progressive phases calculated geometrically from the intended steering direction and frequency. The phase values include the above-described additional element-wise phase calibration. The calculated phase values are also discretized to match those of the 5-bit phase shifters.

The far-field patterns for each prototype are measured using the near-field planar scanner. The near-field data is measured for each beam steering direction θ at 0°, 30°, 45°, and 60° in the E-, H-, and D-planes. The measurements are performed at 24.0, 26.5, 28.0, and 29.5 GHz. Prototype 1 is measured only at the two lower frequency points and Prototype 2 at the three highest frequency points. The far-field results present the absolute realized gain. The measured realized gain in the broadside direction is up to 36.6 dBi when the amplifier gain is 18 dB.

The simulation and measurement results from the 8 × 8 discrete array are shown in Fig. 14. The results are arranged in the order of the angle ϕ (H-plane 0°, D-plane 45°, and E-plane 90°), the prototype, and the corresponding frequency.

Prototypes 1 and 2 should have an identical relative performance at 26.5 GHz (columns 2 and 3 in Fig. 14) since these prototypes ideally have an identical PCB and 3-D-printed antenna array with the RFIC being the only difference. In practice, the bottom face (the face attached to the PCB) of the 3-D-printed antenna block had to be resurfaced with a milling machine [see Figs. 8(b) and (c) and 9(b)] due to manufacturing defects. The slightly altered antenna structures affect the impedance matching, resulting in amplitude variations over frequency and beam steering angles. Despite this, the beam steering results along with the measured gain towards the broadside direction (see Fig. 15) demonstrate the overall functionality of the prototypes.

C. Thermal Measurements

Thermal images of the prototype are taken under three different configurations. The RF-PCB without the 3-D-printed

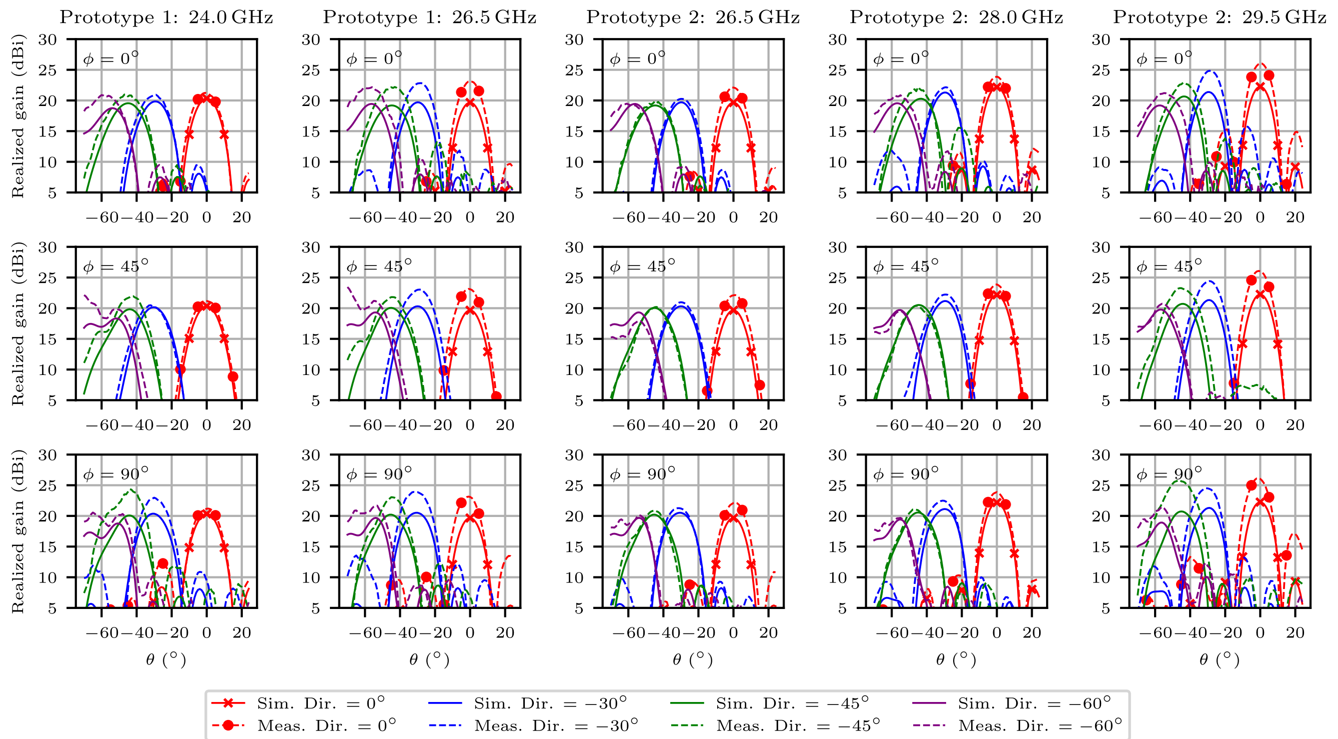

Fig. 14. Simulated (solid lines) and measured (dotted lines) far-field patterns excluding vector modulator gain are shown for Prototype 1 (24.0 and 26.5 GHz) and Prototype 2 (26.5, 28.0, and 29.5 GHz).

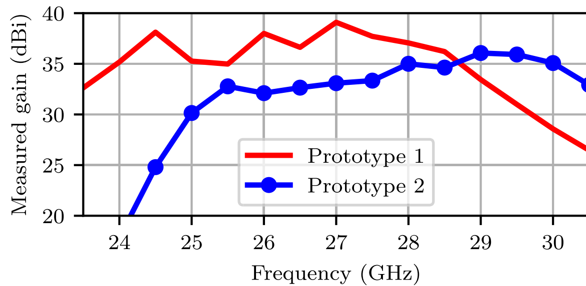

Fig. 15. Measured broadside gain (dBi) of Prototypes 1 and 2 with approximate amplifier gain 20 and 17 dB, respectively.

antenna [see Fig. 16(a)], the RF-PCB and the 3-D-printed antenna with forced convection by a cooling fan [see Fig. 16(b)], and the RF-PCB with the 3-D-printed antenna and the circulating cooling liquid [see Fig. 16(c)]. The images disclose the heat production and thermal challenges in the highly integrated active antennas. In the standby mode, the produced heat is minimal, and there is only a negligible increase in temperature. The heat generation increases significantly in the RX (receive) mode. The RF-PCB without the 3-D-printed antenna heats up to 84 °C in the RX mode. The prototype with forced convection is manageable at 47 °C, and with water cooling the temperature drops to 35 °C. In the TX mode, the RF-PCB-only temperature increases rapidly beyond the operating temperature, and a steady state is not possible at all. The RF-PCB temperature with forced convection is measured to be 80 °C. The RFICs are hotter than the back side of the PCB, and the solution leaves no room for the expansion of the array. The prototype temperature remains below 50 °C using liquid cooling, and no major heat build-up can be seen.

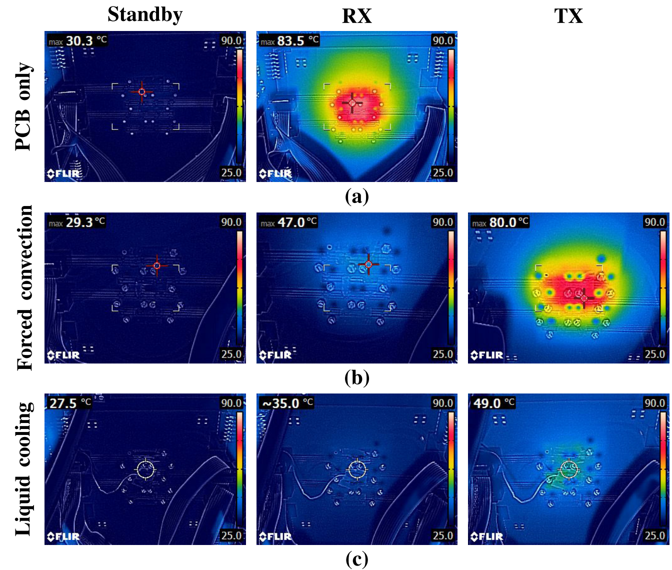

Fig. 16. Thermal images from the back side of the PCB. (a) PCB only, (b) PCB and 3-D-printed antenna with forced convection, and (c) PCB and 3-D-printed antenna with coolant circulation are listed top-down. Standby, RX, and TX functions are listed from left to right.

The relationship between dissipated power and the coolant flow rate is studied during the near-field measurement campaign. The inflow and outflow coolant temperatures are measured along with the PCB hot spot. The power dissipation is changed by adjusting the number of active TX channels. The steady-state temperatures are recorded at various power levels and coolant flow rates. Fig. 17 shows the temperature measurement results indicating the effectiveness of liquid cooling.

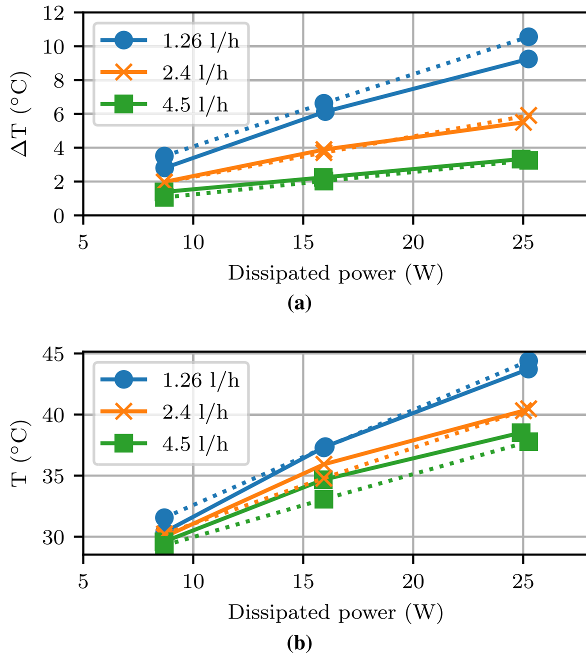

Fig. 17. (a) Temperature difference between ingoing and outgoing cooling water. (b) PCB hot-spot temperature as a function of dissipated power for three different flow rates. The simulation results are presented with dotted lines and the measurement results with solid lines. The ambient temperature is 24 °C.

The simulations were also done with hypothetical RFICs to find out the maximum dissipation power that the prototype can manage. With a 10 l/h flow rate and 65 W combined dissipated power level, the RFICs internal temperature is approximately 84 °C. At this power level, the RFIC's internal temperature differential is significant as the PCB temperature is only 53 °C. This demonstrates that liquid cooling is not the only limiting factor with high power levels. The differential between the RFICs' internal temperature and the immediate surrounding environment temperature (e.g., PCB or 3-D-printed antenna) has to be accounted for in the temperature calculations.

D. Back-Pressure

The coolant channel resists the coolant flow, which creates a pressure difference between the inflow and outflow of a cooling channel. This can impose a design constraint as the array size increases or a higher flow is needed. Both cases require a higher inflow pressure to sustain the operation. The pressure difference is measured using T-junctions before and after the prototype with transparent vertical open-ended tubes. During no flow, the surface levels in both tubes are at the same height. As the flow increases, the prototype restricts the flow which can be seen as uneven water levels between the vertical tubes. The measurement setup includes 75 cm of additional 3-mm inner-diameter tubing to connect the four channels, which is not included in the ideal simulation model. Fig. 18 shows the relationship between back-pressure and flow rate. The simulations and measurements show a similar trend and level over the entire flow rate. The back-pressure is below 2.5 kPa for flow rates under 5 l/h. The back-pressure of the 75-cm long 3-mm inner-diameter reference tube was measured

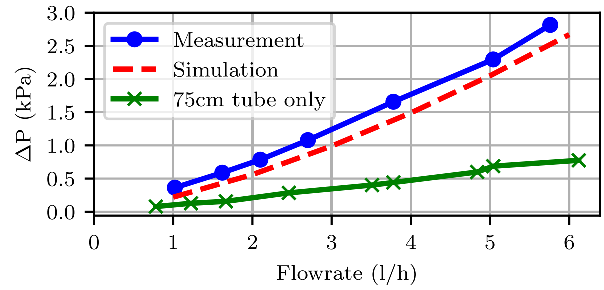

Fig. 18. Back-pressure as a function of the flow rate of the cooling channel.

separately. The measurements show that the majority of the back-pressure drop takes place in the 3-D-printed antenna.

V. Discussion

As seen in Fig. 16(a), the use of RFICs in PCB antennas without a separate cooling structure is impractical. Thermal management is an important part of an active antenna design. The liquid-cooled antenna prototype is presented to solve this problem. The liquid cooling channels in this prototype are daisy-chained externally for the simplicity of the measurement setup. The thermal conduction from the RFIC to the cooling liquid is verified with the PCB backside surface temperature and coolant inflow and outflow temperature measurements. The thermal simulation results agree with the measurements. The PCB backside temperature remained under 50 °C even in the TX mode. When these full-array temperatures are compared to the block approximation in Section II-D, the temperatures are lower due to the additional cooling from the PCB and increased surface area from the Vivaldi structure. If increased cooling is required, additional cooling capacity can be introduced in the prototype by enlarging the cooling channel size. Fig. 2(a) shows that the cooling channel can be expanded in width and height without any effect on the RF side.

The key point for the scalability of the cooling solution is the easy parallelization of the structure. The scaling limitations are set by a single coolant channel that can be parallelized for a 2-D-antenna array. Parallel isolated cooling channels are an easy way to increase cooling capacity. The design also enables higher RF output power in future applications due to the more efficient thermal dissipation. Since the coolant pump and heat exchanger are not part of the design, we do not consider these as design constraints.

An estimate can be made for the antenna array scaling based on the 4.5 l/h flow-rate measurements (see Fig. 17). The estimated temperature budget is calculated from the typical maximally allowed RFIC temperature (85 °C), the temperature difference between the RFIC and PCB hot spot (15 °C), the temperature difference between the hot spot and the cooling water (15 °C), and the ambient temperature (25 °C). Thus, the coolant temperature can be 30 °C above the ambient before the RFIC overshoots the typical maximum temperature. 16 RFICs increased the coolant temperature by 3.3 °C [see Fig. 17(a)]. When the convective heat dissipation into the air is compensated, the calculated coolant temperature increase is 5.0 °C for the 16 RFICs. Thus, a single channel should

be sufficient for 96 (6 × 16) RFICs. Hence, with parallel cooling channels, a 192 × 192-element antenna array could be realized.

The antenna array is also scalable from the RF point of view. As evident from Fig. 9(c), the actual antenna module consists of a 2 × 2 antenna array with an RFIC and dc bypass capacitors in the middle. All the necessary parts are confined within the outline of the 2 × 2 antennas. Scaling of the antenna array is straightforward since modules can be stacked to provide the specified array size, and the necessary feed network can be routed between the modules. The proposed prototype is a 4 × 4 configuration of these modules.

The antenna array utilizes a linear-polarized Vivaldi array to produce a single polarization. Expanding the design to a dual-polarized version is not trivial and should be studied further in the future.

The effective isotropic radiated power (EIRP) is calculated based on the measured broadside gain with de-embedded vector modulators and feed network shown in Fig. 15. The RFIC 1-dB output compression point is 15.5 dBm per channel and 64 channels yield the EIRP between 54.8 and 59.7 dBm.

VI. Conclusion

The active electronics in modern millimeter-wave antenna arrays present a serious heat-dissipation problem. The scaling of active antenna arrays and increased RF output power require effective cooling solutions. To address this, a compact and scalable 8 × 8 antenna array design with liquid cooling is proposed. The design utilizes only one side of the PCB and a 3-D-printed metal antenna array. In this way, the other side of the PCB can be allocated to other functionalities facilitating compactness and high integration. The prototype has an operational bandwidth of 24.0–29.5 GHz and beam-steering capability up to 57°. The EIRP of the prototypes is up to 59.7 dBm. The simulations and measurements confirm the functionality of the prototype. The cooling of the prototype is provided by the 3-D-printed antenna itself with integrated coolant channels. This solution provides sub-50 °C operating temperatures at 25.3 W power usage and leaves the back side of the PCB to be used for power supplies, signal processing, and so on. The RF and thermal simulations are in agreement and indicate high scalability of the design.

Acknowledgment

The authors would like to thank D.Sc. (Tech.) Markku Lahti from the VTT Technical Research Center of Finland Ltd., and the Lic.Sc. (Tech.) Matti Vaaja from the School of Electrical Engineering, Aalto University for their contribution.

References

[1] Qualcomm and Nokia. (2017). *Making 5G a Reality: Addressing the Strong Mobile Broadband Demand in 2019 & Beyond*. [Online]. Available: https://www.qualcomm.com/content/dam/qcomm-martech/dm-assets/documents/whitepaper_-_making_5g_a_reality_-_addressing_the_strong_mobile_broadban_1.pdf

[2] Nokia. (2017). *5G Technology Components*. [Online]. Available: https://resources.ext.nokia.com/asset/201378

[3] K. Kibaroglu, M. Sayginer, and G. M. Rebeiz, "A low-cost scalable 32-element 28-GHz phased array transceiver for 5G communication links based on a 2 × 2 beamformer flip-chip unit cell," *IEEE J. Solid-State Circuits*, vol. 53, no. 5, pp. 1260–1274, Aug. 2018.

[4] K. Kibaroglu, M. Sayginer, T. Phelps, and G. M. Rebeiz, "A 64-element 28-GHz phased-array transceiver with 52-dBm EIRP and 8–12-Gb/s 5G link at 300 meters without any calibration," *IEEE Trans. Microw. Theory Techn.*, vol. 66, no. 12, pp. 5796–5811, Dec. 2018.

[5] G. Raney, B. Unruh, R. Lovestead, and B. Winther, "64-element 28 gigahertz phased array 5G prototyping platform," in *Proc. 11th Global Symp. Millim. Waves (GSMM)*, May 2018, pp. 1–4.

[6] X. Gu, D. Liu, and B. Sadhu, "Packaging and antenna integration for silicon-based millimeter-wave phased arrays: 5G and beyond," *IEEE J. Microw.*, vol. 1, no. 1, pp. 123–134, Jan. 2021.

[7] K. K. W. Low, S. Zihir, T. Kanar, and G. M. Rebeiz, "A 27–31-GHz 1024-element Ka-band SATCOM phased-array transmitter with 49.5-dBW peak EIRP, 1-dB AR, and ±70° beam scanning," *IEEE Trans. Microw. Theory Techn.*, vol. 70, no. 3, pp. 1757–1768, Jan. 2022.

[8] Q. Ma et al., "A 5G 25–29 GHz 64-element phased-array with 49–52 dBm EIRP, integrated up/down-converter and on-chip PLL," in *IEEE MTT-S Int. Microw. Symp. Dig.*, Jun. 2021, pp. 854–857.

[9] A. J. Van Den Biggelaar, C. J. C. Vertegaal, U. Johannsen, A. B. Smolders, and M. Geurts, "On the design and calibration of a 5G millimeter-wave dual-polarized active phased array," in *Proc. IEEE-APS Topical Conf. Antennas Propag. Wireless Commun. (APWC)*, Aug. 2021, pp. 055–060.

[10] R. W. Kindt and J. T. Logan, "Benchmarking ultrawideband phased antenna arrays: Striving for clearer and more informative reporting practices," *IEEE Antennas Propag. Mag*, vol. 60, no. 3, pp. 34–47, Apr. 2018.

[11] H. Kahkonen, J. A.-Laurinaho, and V. Viikari, "Dual-polarized Ka-band Vivaldi antenna array," *IEEE Trans. Antennas Propag.*, vol. 68, no. 4, pp. 2675–2683, Apr. 2020.

[12] A. Alhamed, O. Kazan, G. Gultepe, and G. M. Rebeiz, "A multiband/multistandard 15–57 GHz receive phased-array module based on 4 × 1 beamformer IC and supporting 5G NR FR2 operation," *IEEE Trans. Microw. Theory Techn.*, vol. 70, no. 3, pp. 1732–1744, Mar. 2022.

[13] H. Kähkönen, J. Ala-Laurinaho, and V. Viikari, "A modular dual-polarized Ka-band Vivaldi antenna array," *IEEE Access*, vol. 10, pp. 36362–36372, 2022.

[14] J. Sinnhuber and B. Kaehs, "Efficiency in broadcasting, definition and measurement of transmitter efficiency," Rohde & Schwarz, Munich, Germany, Tech. Rep., 2.2016–01.00, Feb. 2016. [Online]. Available: https://cdn.rohde-schwarz.com/pws/solution/broadcasting/content_distribution/terrestrial_ transmission/R_S_Whitepaper_Efficiency_in_broadcasting.pdf

[15] J. Hesselbarth, "Eight-port radiator element for millimeter-wave antenna array," in *Proc. Eur. Microw. Conf. Central Eur. (EuMCE)*, May 2019, pp. 411–414.

[16] M. Lippoldt and J. Hesselbarth, "High-efficiency and broadband surface-mount antenna array concept and prototype," *IEEE Antennas Wireless Propag. Lett.*, vol. 19, no. 8, pp. 1425–1428, Aug. 2020.

[17] S. Holzwarth, O. Litschke, W. Simon, H. Fischer, J. Kassner, and A. Serwa, "Highly integrated 8 × 8 antenna array demonstrator on LTCC with integrated RF circuitry and liquid cooling," in *Proc. 4th Eur. Conf. Antennas Propag.*, 2010, pp. 1–4.

[18] B. Tomasic, D. Wisniewski, R. Schmier, T. Steffen, and G. Phillips, "Cold plate design, fabrication, and demonstration for high-power Ka-band active electronically scanned arrays," in *Proc. IEEE Int. Symp. Antennas Propag. USNC-URSI Radio Sci. Meeting*, Jul. 2019, pp. 35–36.

[19] J. Qian, M. Tang, Y.-P. Zhang, and J. Mao, "Heatsink antenna array for millimeter-wave applications," *IEEE Trans. Antennas Propag.*, vol. 68, no. 11, pp. 7664–7669, Nov. 2020.

[20] L. Zhou, M. Tang, J. Qian, Y.-P. Zhang, and J. Mao, "Vivaldi antenna array with heat dissipation enhancement for millimeter-wave applications," *IEEE Trans. Antennas Propag.*, vol. 70, no. 1, pp. 288–295, Jan. 2022.

[21] R. Banerjee, S. Kumar Sharma, J.-C. Samuel Chieh, and R. Farkouh, "Investigations of heat sink property of a novel dual linear polarized low cross-polarization X-band phased array antenna employing silicon RFICs-based beamforming network," *IEEE Open J. Antennas Propag.*, vol. 3, pp. 523–537, 2022.

[22] S. M. Duffy, G. A. Brigham, K. B. Newman, and J. S. Herd, "Stepped notch antenna array used as a low thermal resistance heat sink," in *Proc. IEEE Antennas Propag. Soc. Int. Symp. (APSURSI)*, Jul. 2013, pp. 622–623.

[23] M. de Kok, A. Bart Smolders, C. J. C. Vertegaal, and U. Johannsen, "Active Ka-band open-ended waveguide antenna with built-in IC cooling for use in large arrays," in *Proc. 18th Eur. Radar Conf. (EuRAD)*, Apr. 2022, pp. 86–89.

[24] ETSI. (2018). *3GPP TS 38.101-2 Version 15.3.0 Release 15, 5G;NR;User Equipment (UE) Radio Transmission and Reception; Part 2: Range 2 Standalone*, [Online]. Available: https://www.etsi.org/deliver/etsi_ts/138100_138199/13810102/15.03.00_60/ts_13810102v150300p.pdf

[25] M. Skolnik, *Radar Handbook*, 2nd ed. New York, NY, USA: McGraw-Hill, 1990.

[26] Y. Yang, Y. Wang, and A. E. Fathy, "Design of compact Vivaldi antenna arrays for UWB see through wall applications," *Prog. Electromagn. Res.*, vol. 82, pp. 401–418, 2008.

[27] Digital Metal. (2021). *DM Cu Material Datasheet*. [Online]. Available: https://digitalmetal.tech/wp-content/uploads/2021/02/DIM0095_Datasheet_DMCu.pdf

[28] Digital Metal. (2021). *Surface Quality*. [Online]. Available: https://digitalmetal.tech/order-components/surface-quality/

[29] W. L. Stutzman and G. A. Thiele, *Antenna Theory and Design*. Hoboken, NJ, USA: Wiley, 2012.

[30] J. Haarla, "Manufacturing files for the antenna array PCB," Aalto Univ., Espoo, Finland, Tech. Rep., 2022. [Online]. Available: https://ieee-dataport.org/documents/manufacturing-files-antenna-array-pcb, doi: 10.21227/8bqy-mn70.

[31] P. Kosky, R. Balmer, W. Keat, and G. Wise, *Exploring Engineering: An Introduction to Engineering and Design*. Amsterdam, The Netherlands: Elsevier Science, 2021.

[32] R. Mailloux, *Phased Array Antenna Handbook*, 2nd ed. Norwood, MA, USA: Artech House, 2005.

Jaakko Haarla received the B.Sc. (Tech.) degree in electronics and the Diploma Engineer (M.Sc.) degree in radio science and engineering from Aalto University, Espoo, Finland, in 2015 and 2017, respectively.

Since 2016, he has been with the Department of Electronics and Nanoengineering, Aalto University. His current research interests include phased antenna arrays, thermal management, antenna measurements, and RFIC integration at millimeter waves.

Juha Ala-Laurinaho received the Diploma Engineer (M.Sc.) degree in mathematics and the D.Sc. (Tech.) degree in electrical engineering from the TKK Helsinki University of Technology, Espoo, Finland, in 1995 and 2001, respectively.

He was with Aalto University, formerly TKK, serving with the Radio Laboratory, from 1995 to 2007, with the Department of Radio Science and Engineering, from 2008 to 2016, and at present with the Department of Electronics and Nanoengineering. He is currently working as a Staff Scientist. He has been a Researcher and Project Manager in various millimeter-wave technology-related projects. His current research interests include antennas and antenna measurement techniques for millimeter and submillimeter waves and millimeter-wave imaging.

Ville Viikari (Senior Member, IEEE) received the M.Sc. (Tech.) and D.Sc. (Tech.) (Hons.) degrees in electrical engineering from the Helsinki University of Technology (TKK), Espoo, Finland, in 2004 and 2007, respectively.

From 2001 to 2007, he was with the Radio Laboratory, TKK (now part of Aalto University), where he studied antenna measurement techniques at submillimeter wavelengths and antenna pattern correction techniques. From 2007 to 2012, he was a Research Scientist and a Senior Scientist with the VTT Technical Research Center, Espoo, where his research included wireless sensors, RFID, radar applications, MEMS, and microwave sensors. He was appointed as an Assistant Professor with Aalto University, in 2012. He is currently a Professor and the Deputy Head of the Department with the School of Electrical Engineering, Aalto University, Espoo. He has authored or coauthored more than 90 journal articles and 100 conference papers. He is an inventor with 16 granted patents. His current research interests include antennas for mobile devices and networks, antenna clusters and coupled arrays, RF-powered devices, and antenna measurement techniques.

Dr. Viikari is a Regional Delegate of EurAAP. He was the recipient of the Young Researcher Award of the Year 2014, presented by the Finnish Foundation for Technology Promotion, and the IEEE Sensors Council 2010 Early Career Gold Award.